PREPRINT

EXPERIMENTAL AND NUMERICAL INVESTIGATION OF THE FLOW IN A TRAILING EDGE RIBBED INTERNAL COOLING PASSAGE

Seungchan Baek
Department of Mechanical
& Aerospace Engineering
Seoul National University
Seoul, Republic of Korea

Sangjoon Lee
Department of Mechanical
& Aerospace Engineering
Seoul National University
Seoul, Republic of Korea

Wontae Hwang
Institute of Advanced
Machines and Design
Department of Mechanical
& Aerospace Engineering
Seoul National University
Seoul, Republic of Korea

Jung Shin Park
Thermal and Fluid
Research Team
DOOSAN HEAVY
INDUSTRIES & CO., LTD

ABSTRACT

The flow field in a ribbed triangular channel representing the trailing edge (TE) internal cooling passage of a gas turbine high pressure turbine (HPT) blade is investigated via Magnetic Resonance Velocimetry (MRV) and Large Eddy Simulation (LES). Results are compared to a baseline channel with no ribs. LES predictions of the mean velocity fields are validated by the MRV results. In the case of the baseline triangular channel with no ribs, the mean flow and turbulence level at the sharp corner are small, which would correspond to poor heat transfer in an actual trailing edge. For the staggered ribbed channel, turbulent mixing is enhanced, and flow velocity and turbulence intensity at the sharp edge increase. This is due to secondary flow induced by the ribs moving toward the sharp edge in the center of the channel. This effect is expected to enhance internal convective heat transfer for the turbine blade trailing edge.

INTRODUCTION

As the demand for turbine efficiency and power increases, the design of advanced high-pressure turbine blades has improved significantly over the past several decades. Various internal and external cooling techniques are being applied to gas turbine blade designs, so the blades can reliably withstand the high turbine inlet temperatures required for high efficiency. At the blade trailing edge, it is challenging to design an internal cooling flow path that can provide adequate internal cooling, due to its strict geometrical constraints. In order to minimize aerodynamic losses, trailing edge internal channels generally have a high aspect ratio (typically between 4 and 7), and a sharp apex angle toward the blade trailing edge, which inhibits heat transfer and can potentially cause severe thermal stresses [1].

In order to overcome these thermal issues of sharp trailing edges, many recent designs have adopted cutback trailing edge slots that avoid a sharp edge and allow the coolant to externally mix with the surrounding hot gas. Many studies have been conducted utilizing a variety of techniques. Benson et al. [2-3] analyzed trailing edge cutback film cooling by magnetic resonance velocimetry (MRV) for various geometries and parameters such as Reynolds number and blowing ratio. Chen et al. [4] observed flow in the wake of a cutback trailing edge by particle image velocimetry (PIV). Martini et al. [5-6] examined film cooling performance of a cutback trailing edge with various internal cooling designs via experiments and numerical simulations. Mucignat et al. [7] evaluated the flow characteristics inside a rotating trailing edge by PIV and Reynolds averaged Navier Stokes (RANS) simulations. Armellini et al. [8-9] analyzed the characteristics of flow and heat transfer in a rib-roughened trailing edge channel with crossing-jets. Schneider et al. [10] assessed the performance of standard RANS turbulence modeling for predicting heat transfer in a cutback trailing edge, and analyzed the coherent structure in the wake of the trailing edge utilizing high fidelity large eddy simulations (LES).

Notwithstanding the many studies on cutback trailing edge slots, these designs still tend to suffer from thermal stresses due to inadequate cooling. Also in some cases (for example, latter stages of the turbine) external cooling may not be the optimal solution, and internal cooling only might be desired. Thus, it is important to find a way to improve internal cooling.

A small number of studies have focused on the flow structures and heat transfer in the narrow corners of isosceles triangular channels. Eckert and Irvine [11] experimentally examined the heat transfer coefficient and friction factor in triangular channel flow with a narrow apex angle of 11.5°. Hiromoto et al. [12] analyzed mass transfer for a triangular channel with the same apex angle as Eckert. They observed laminar flow behavior at the sharp corner, which is responsible for locally reduced heat transfer. A similar phenomenon was

analyzed computationally by Daschiel et al [13]. This study was performed to supplement Eckert's experimental results with DNS data of a triangular channel flow at Re = 4,500. Similar to the study done by Eckert, heat transfer was reduced because of damped turbulence. These findings suggest that the flow and turbulence need to be increased in the narrow corner to enhance heat transfer.

The aim of this paper is to examine how ribs modify the flow field within a triangular cooling channel. Methods employed are magnetic resonance velocimetry (MRV) and large eddy simulation (LES). MRV can measure the 3 dimensional 3 component (3D3C) mean velocity field in complex geometries using an MRI scanner [2-3]. By comparing the experimental and numerical data, LES results will first be validated, and then further utilized to enhance understanding of the 3D turbulent flow structure.

NOMENCLATURE

AR	Aspect ratio (W/H)
CFD	Computational Fluid Dynamics
CFL	Courant–Friedrichs–Lewy condition
DNS	Direct numerical simulation
D_h	Hydraulic diameter
FOV	Field of View
FVM	Finite Volume method
f	friction factor
HPT	High pressure turbine
H	channel height
h	rib height
L	Centerline length
l	rib length
L_e	Entrance length
LES	Large eddy simulation
Mol	Molarity
MRI	Magnetic Resonance Imaging
MRV	Magnetic Resonance Velocimetry
PIV	Particle Imaging Velocimetry
p	rib pitch
Q	Volumetric flow rate
RANS	Reynolds Averaged Navier-Stokes
Re	Reynolds number ($D_h U_b /v$)
RMS	Root mean square
SNR	Signal to noise ratio
TE	Trailing edge
U_b	Bulk velocity
Venc	Velocity encoding
W	channel width
w	rib width
α	Angle of attack
σ_n	Standard deviation of measurement
δ_A	Area uncertainty of flow domain
δ_V	Velocity uncertainty
δ_Q	Volumetric flow rate uncertainty
θ	Apex angle

EXPERIMENTAL METHOD

A schematic of the overall experimental setup is shown in figure 1. The flow loop consists of a water tank, parallel connected pumps, diaphragm valve, paddlewheel flowmeter, and test section. A bypass loop is installed to allow the desired flow rate to be controlled through main and bypass valves. The pumps run at full power. The flowrate entering the test section is measured by the paddlewheel flowmeter. A 3T Siemens MAGNETOM Trio MRI scanner at Seoul National University Hospital is used with a phased array torso coil, as shown in figure 2. All of the components in the MRI scan room are limited to materials that are not affected by the magnetic field.

Figure 3 shows details of the experimental test rig. The flow conditioning section, adapted from Benson et al. [3], contains multiple grids to create a uniform flow. The cross section is expanded from the 1-1/2" (38.1mm) inlet hose to the 6" x 6" (152mm x 152mm) square plenum. At the end of the square plenum, a triangular bell mouth inlet is installed to provide a uniform inlet flow to the test section, without a vena contracta. The test section is robustly designed to test various types of turbulators, by changing the pressure and suction side plates of the model. The straight triangular test section, which is scanned in the MRI machine, is made using transparent acrylic material. This is to allow for visual checks of bubbles or foreign material, which can cause errors in the measurements.
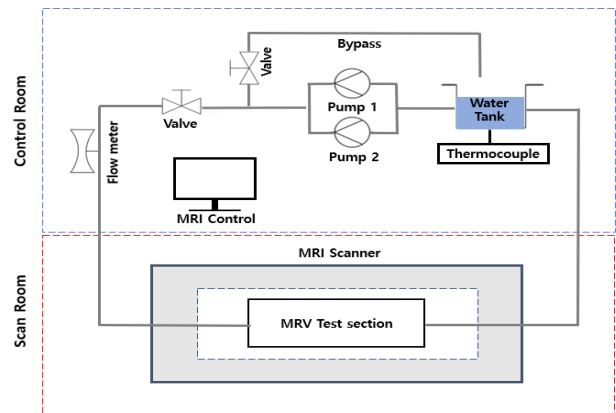

Figure 1. Flow diagram.
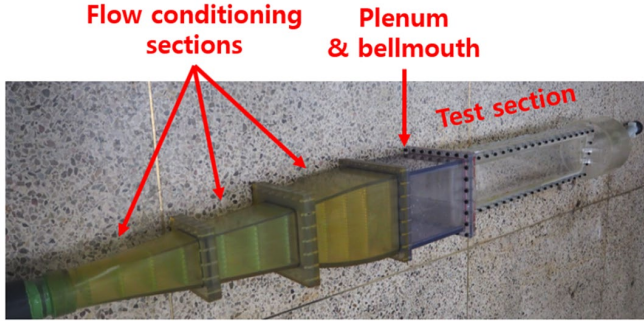

Figure 2. Test setup in the MRI scanner.

Figure 3. Water channel installed in the MRI room

The test geometries of the baseline and ribbed triangular channels are depicted in figures 4, 5 and, 6. The details of the configuration are outlined in Table 1. The ribbed triangular channel has the same overall channel shape as the baseline case, with the exception of staggered 45° ribs on the pressure and suction sides.
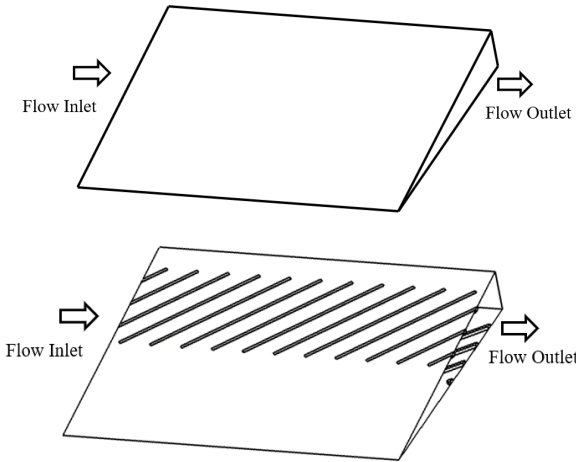

**Figure 4. Right triangular channels.
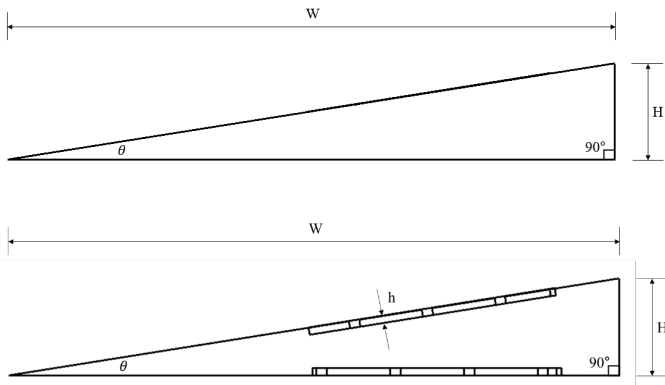(Top) baseline, (bottom) ribbed.**

**Figure 5. Cross section of triangular channels.
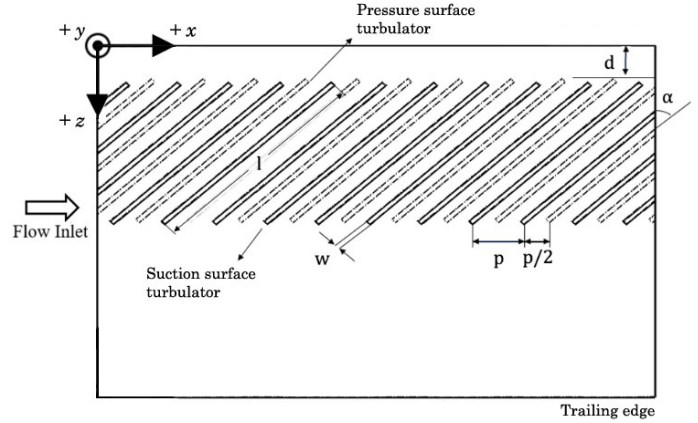(Top) baseline, (bottom) ribbed.**

Figure 6. Rib geometry in the channel

Table 1. Cross-sectional geometry and rib parameters.

Cross-sectional geometry	
Sectional shape	Right triangle
Apex angle (θ)	9.0°
Channel width (W)	108 mm
Channel height (H)	17.0 mm
Aspect ratio (W/H)	6.3
Hydraulic diameter (D_h)	23.4 mm
Rib information	
Rib width (w)	1.3 mm
Rib pitch (p)	13 mm
Rib length (l)	60.8 mm
Rib height (h)	1.3 mm
Pitch/height (p/h)	10
Distance from the vertical plate (d)	10.1 mm
Angle of attack (α)	45°
Shape of rib end	90° edges

The field of view (FOV) of the measurement domain was set as 72 mm (x)×44 mm (y)×128 mm (z), toward the end of the channel. Since scan time is proportional to scan length, this length was chosen to allow at least one full rib pattern to be imaged. The spatial resolution was set at 0.5 mm (y)×0.5 mm (z) in the cross section, in order to resolve the rib height and the sharp edge, without an exorbitantly long scan time. The resolution for the streamwise direction, which is likely not to change abruptly (especially for the baseline case), was set to 1 mm (x) in order to also minimize scan time. The entrance length is estimated according to the entrance length of pipe flow $L_e = 16D_h = 374$ mm [14]. The measurement domain is 500 mm from the inlet for both baseline and ribbed channels. A total of 44 pairs of ribs were installed in a staggered pattern on each plate, starting 10 mm away from the inlet so that the flow would be fully developed at the measurement location.

Each scan took 20.5 minutes. A total of seven 'flow on' scans are obtained, and five 'flow off' scans are taken in between to eliminate temporally changing background artifacts. The total test time was approximately 6 hours. The ensemble averaged

background 'flow off' scans are subtracted from the ensemble averaged 'flow on' scans to obtain time averaged mean velocity fields with 1.6 million velocity vectors.

Velocity encoding (Venc), which can be considered the dynamic range, is set at 2,500 mm/s in order not to exceed the maximum velocity. Working fluid used in the experiment is 0.04 M copper sulfate aqueous solution, which is made by adding copper sulfate pentahydrate (Cu_2SO_4) to deionized water. The hydrodynamic properties of 0.04 M solution are not significantly different from those of universal water, and it has been shown in prior studies that this concentration results in optimal signal to noise ratio (SNR) for MRI scans [15]. Two flow conditions are tested; 65.2 L/min for the baseline channel and 46.0 L/min for the ribbed channel, which correspond to Re = 20,000 and 14,000 respectively. These conditions were requested from Doosan Heavy Industries. The average fluid temperature is maintained at 23°C in order to keep the fluid viscosity constant. Temperature rise due to continuous pump operation is controlled to be within ±1°C using several ice bottles. Experimental parameters are summarized in Table 2.

Table 2. Experimental parameters.

Imaging Parameters	
FOV ($x{\times}y{\times}z$)	72 mm×44 mm×128 mm
Spatial resolution ($x{\times}y{\times}z$)	1 mm×0.5 mm×0.5 mm
Venc	2,500 mm/s
Scan time for single run	20.5 min
Number of repetitions	7 'flow on' scans 5 'flow off' scans
Number of velocity vectors	1.6 x 10^6
Flow Parameters	
Fluid	0.04 M copper sulfate water solution
Temperature	23°C
Volumetric flow rate	65.2 L/min (baseline), 46.0 L/min (ribbed)
Reynolds number	20,000 (baseline), 14,000 (ribbed)

Finally, the average velocity is calculated by scaling the average 'flow on' – 'flow off' phase to the Venc. The overall procedure to estimate velocity uncertainty follows that of Elkins et al. [16]. The standard deviation of velocity is estimated as [17]

$$\sigma_n = \frac{\sqrt{2}}{\pi}\frac{\text{Venc}}{\text{SNR}} \qquad (1)$$

SNR is calculated from the mean signal value of the region of interest (ROI) after subtracting the mean background noise, using the MRI magnitude images. ROI refers to the flow region, which is determined by the presence of signal due to copper sulfate. Segmentation of the ROI and background is conducted based on a threshold value of the magnitude intensity. In order to evaluate the velocity uncertainty at a confidence interval of 95%,

the student t-distribution is used because of the limited number of tests (N=7) [18].

$$\delta_V = 2.447\frac{\sigma_n}{\sqrt{N}} \qquad (2)$$

In Table 3, the overall velocity uncertainty is given based on Equation (1) and (2). Comparing the SNR for the baseline and the ribbed channel, we can see that the SNR is higher for the baseline channel, even though the maximum velocity is higher. In the ribbed channel, turbulence due to the ribs generates noise in the MRI signal. Bruschewski et al. [19] artificially added noise that can be assumed to be due to turbulence error in k-space data, to show how errors resulting from turbulence propagate. Because the turbulence induced errors in the ribbed channel are larger, the SNR is lower.

Based on the uncertainty for velocity measurement, flow rate uncertainty is estimated. The flowrate uncertainty was analyzed with reference to Benson et al [3]. In general, the volumetric flow rate can be expressed as Q = A·V, so that the uncertainty for flow rate can be expressed as a combination of uncertainty for flow area and velocity. It can be expressed as a root-sum-of-square formula (Equation 3). The uncertainty of the velocity was estimated by the above method, and the uncertainty of the flow area was obtained by subtracting the minimum possible area from the maximum possible area due to voxels where fluid and plastic model coexist. This influence is called the partial volume effect.

$$\delta_Q = \sqrt{\left(\frac{\partial Q}{\partial V}\cdot\delta_V\right)^2 + \left(\frac{\partial Q}{\partial A}\cdot\delta_A\right)^2}$$
$$= \sqrt{(A\cdot\delta_V)^2 + (V\cdot\delta_A)^2} \qquad (3)$$

The flowmeter uncertainty is obtained using the bucket and stopwatch method.

The uncertainty of flow rate is given in Table 3. Uncertainty from MRV results are 9.8% of the mean flow rate for the baseline channel, and 9.3% for the ribbed channel. However, the flow rate discrepancy between MRV results and flow meter for the baseline and ribbed channel is only 0.3% and 0.15%, respectively.

Table 3. Velocity uncertainty and flow rate error for the baseline and ribbed channel.

	Baseline channel	Ribbed channel
Max. velocity	1.31 m/s	1.13 m/s
SNR	15.45	13.41
MRV velocity uncertainty	± 0.073 m/s (± 5.1%)	± 0.078 m/s (± 6.9%)
Flow rate (flowmeter)	65.3 ± 0.22 L/min	46.0 ± 0.34 L/min
Flow rate (MRV)	65.1 ± 6.37 L/min	45.9 ± 6.02 L/min
Flow rate error	0.3%	0.15%

A 3×3 pixel median filter is applied to the 3D3C mean velocity field to further reduce noise, following the methodology of Benson el al. [3].

NUMERICAL METHOD

The numerical approach in this study utilizes large eddy simulation (LES) with an immersed boundary method (IBM). This numerical approach is based on the finite volume method suggested by Kim et al. [20], using a second-order central difference method for space and a semi-implicit fractional-step method for time. For the subgrid-scale eddy viscosity model, the dynamic subgrid-scale eddy viscosity model with a global model coefficient is used [21]. The governing equations for this approach, thus, are grid-filtered continuity, and Navier-Stokes equations for Newtonian incompressible flow.

At the surface of the channel, which is defined via the immersed boundary, a no-slip condition is applied by implementing the momentum forcing terms. A periodic boundary condition is imposed in the streamwise $(+x)$ direction. The computational domain and the wall structures with mesh details are shown in figure 7. The streamwise domain size is determined as 5 times D_h for the baseline channel, and a single cycle of the rib pattern for the ribbed channel, thus providing a sufficiently long region in which the turbulence can be calculated. It should be noted that Ahn et al. [22], who utilized the same numerical method for analyzing flow in a plane channel roughened by ribs, reported that a computation containing only one pair of ribs resulted in nearly the same time-averaged values of flow quantities as the results of a computation containing three pairs of ribs.
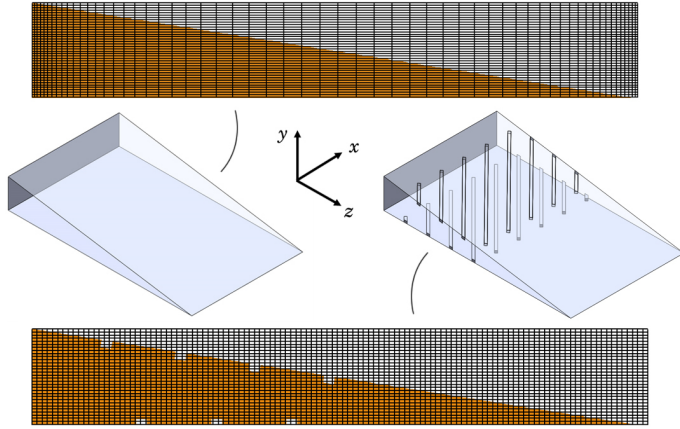

Figure 7. Computational domain of numerical analysis with mesh details. (Left) baseline channel, (right) ribbed channel.

In order to check mesh independency, three different grid systems for each channel are implemented and calculated. Information of the grid system is summarized in Table 4. For the baseline channel, grid points are concentrated near the wall and the sharp corner; thus, the grid interval is smallest near the wall. The Reynolds number for each simulation is the same as the experiment, 20,000 for the baseline channel and 14,000 for ribbed channel. The non-dimensional grid intervals with superscript '+', expressed as $\Delta x_i^+ = u^* \Delta x_i / \nu$, where u^* is the friction velocity, are *a priori* calculated from the Blasius solution [14], meaning that the actual values can be smaller than the Blasius solution because the current channel geometry is non-circular. The resolution of the fine grid system satisfies the requirements of $O(\Delta s^+) \leq 10^2$ and $O(\Delta w^+) \sim 1$ suggested by Davidson [23], where Δs and Δw denote the streamwise and wall-adjacent grid intervals, respectively.

Table 4. Overview of numerical grids to assess mesh independency.

Baseline channel (Re = 20,000)			
Grid cases	Coarse ($96 \times 161 \times 321$)	Medium ($96 \times 321 \times 481$)	Fine ($96 \times 641 \times 576$)
Number of cells	4,961,376	14,822,496	35,444,736
$\Delta x/D_h$ (Δx^+)	0.0521 (60.0)	0.0521 (60.0)	0.0521 (60.0)
$\Delta y/D_h$ (Δy^+)	0.0068 (7.8)	0.0034 (3.9)	0.0017 (2.0)
$\Delta z/D_h$ (Δz^+)	0.0068 - 0.0349 (7.8 - 40.2)	0.0034 - 0.0256 (3.9 - 29.5)	0.0017 - 0.0249 (2.0 - 28.7)
Ribbed channel (Re = 14,000)			
Grid cases	Coarse ($96 \times 96 \times 576$)	Medium ($192 \times 128 \times 768$)	Fine ($192 \times 256 \times 1408$)
Number of cells	5,308,416	18,874,368	69,206,016
$\Delta x/D_h$ (Δx^+)	0.0086 (7.3)	0.0043 (3.6)	0.0043 (3.6)
$\Delta y/D_h$ (Δy^+)	0.0113 (9.5)	0.0085 (7.2)	0.0043 (3.6)
$\Delta z/D_h$ (Δz^+)	0.0119 (10.0)	0.0089 (7.5)	0.0048 (4.1)

The initial flow conditions are first set using parabolic velocity profiles obtained from the laminar solution at Re = 1,000, with superposition of random three-dimensional perturbations of 0.1 U_b. Since a uniform flow rate condition is used as the boundary condition, the bulk velocity U_b is maintained regardless of time. Next, simulations using coarse grids for each channel are carried out for 10,000 timesteps without averaging, in order to reach fully developed turbulent flow. This corresponds to at least 30 turnover times D_h/U_b. The interval of each time step is dynamically determined under the Courant–Friedrichs–Lewy (CFL) condition, such that the maximum CFL number is unity. A decision on whether the flow has become fully developed or not is made based on the observation of the interim flow field and the convergence of the overall shear force acting on the channel. After fully developed velocity profiles for the coarse grids are obtained, these flow fields are interpolated and utilized as initial conditions for the simulations using medium and fine grids, in order to save

computational time. The simulations are then run for 5,000 timesteps, or approximately 10 turnover times, to stabilize the flow fields.

After this, additional calculations of 10,000 and 8,000 timesteps for the baseline and ribbed channel, respectively, are performed to obtain statistics for the turbulent flow. Since the constant time interval condition is applied, the simulations for each case are extended for exactly 20 and 8 turnover times, respectively, with Reynolds time-averaging [14]. Both sampling times are longer than that of Ahn et al. [22], 5 turnover times.

Table 5 shows the friction factors of the triangular channels calculated from the different grid systems above, which are computed from nondimensionalization of pressure loss per streamwise length $\Delta p/\Delta x$ or mean wall shear stress $\overline{\tau_w}$.

$$f = \frac{2 \cdot \Delta p/\Delta x}{\rho U_b^2/D_h} = \frac{8 \cdot \overline{\tau_w}}{\rho U_b^2} \qquad (4)$$

In the case of the baseline channel, the friction factors calculated from the medium and fine grids are considered to be properly calculated according to the Carlson-Irvine correlation [24]. However, the coarse grid considerably underpredicts the friction factor of the baseline channel, -15.7 % compared to the fine grid result. Since the wall-adjacent grid of the coarse grid is located in the overlap layer ($\Delta w^+ = 5 \sim 30$), the coarse grid fails to resolve the flow in the viscous layer ($\Delta w^+ < 5$). On the other hand, the fine grid result shows only a -2.6 % difference from the Carlson-Irvine correlation, which can be explained by the slight geometric discrepancy of the channel. The Carlson-Irvine correlation formula is based on an isosceles triangular channel, while this study analyzes a right triangular channel. Therefore, all the numerical results of the baseline channel hereinafter were calculated by the fine grid structure, since the friction factor shows reasonable and reliable results.

In the case of the ribbed channel, a similar tendency of friction factor appears. However, the discrepancy of friction factor between the grid systems is more severe than the baseline case. This is probably due to the fact that the existence of ribs causes a more complex turbulent flow. It can be seen that the percent difference decreases as the grid becomes fine. Although the friction factor does not seem to be completely converged even at the finest grid structure, 70 million cells was deemed adequate for the ribbed channel in this study, considering the limitation in computational resources.

Table 5. Friction factor for different grid structures.

Baseline channel (Re = 20,000)			
Grid cases	Coarse	Medium	Fine
Friction factor	1.83×10^{-2}	2.10×10^{-2}	2.17×10^{-2}
Difference	- 15.7 %	- 3.2 %	-
Ribbed channel (Re = 14,000)			
Grid cases	Coarse	Medium	Fine
Friction factor	2.13×10^{-2}	2.38×10^{-2}	2.68×10^{-2}
Difference	-20.5 %	-11.2 %	-

Figure 8 illustrates the friction factors obtained from LES, in comparison with previous results. As can be seen, the friction factor is a weak function of Reynolds number and decreases as the Reynolds number increases. The friction factor also highly depends on the channel geometry. In the case of the isosceles triangular channel with apex angle of 9.0°, the friction factor is significantly lower compared to the circular pipe. Compared to the isosceles triangular channel, the centerline asymmetricity of the right triangular channel seems to generate some additional decrease of the friction factor. In addition, after the effect of the difference in Reynolds number is removed by adjusting the friction factor of the baseline channel via the modified Blasius formula with a constant C of 0.258, it can be seen that the friction factor of the ribbed channel is 13.0 % higher than that of the baseline channel.
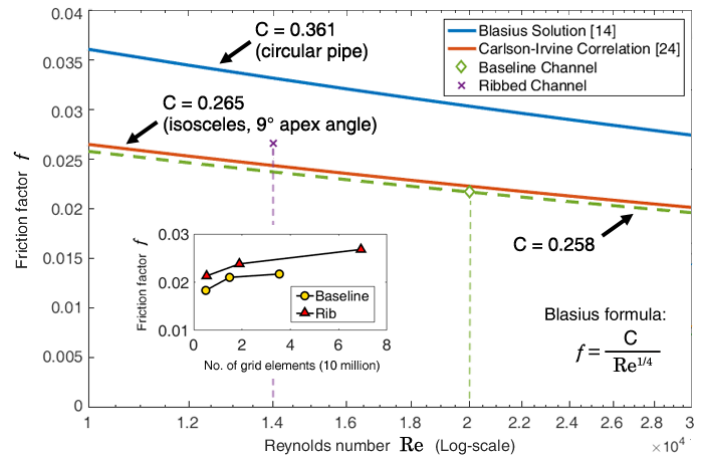

Figure 8. Friction factor in comparison with the Carlson-Irvine correlation and Blasius solution. Subplot shows the convergence of the friction factor with number of cells.

RESULTS AND DISCUSSION
Baseline channel

The baseline triangular channel flow is first analyzed. The mean streamwise velocity contours in the channel cross section obtained by MRV and LES are compared in figure 9. The streamwise flow velocity is maximized near the center of the channel and descends toward the sharp corner as the viscous layer effect becomes dominant throughout the entire flow region. The MRV contour shows a slightly higher streamwise velocity in the middle of the channel, whereas the LES contour shows slightly higher velocity at the right side of the triangle.

Figure 10 shows the normalized streamwise velocity U/U_b profile along the centerline of the baseline channel, which is taken from the narrow apex point to the middle of the opposite side. The length of this centerline is defined as L. Although a slight overshoot of the LES velocity profile is observed near $\tau/L = 0.15$, the overall tendency of the MRV and LES results match fairly well. In particular, it should be noted that both profiles display a sudden drop in the velocity towards the sharp corner where the viscous sublayer dominates.
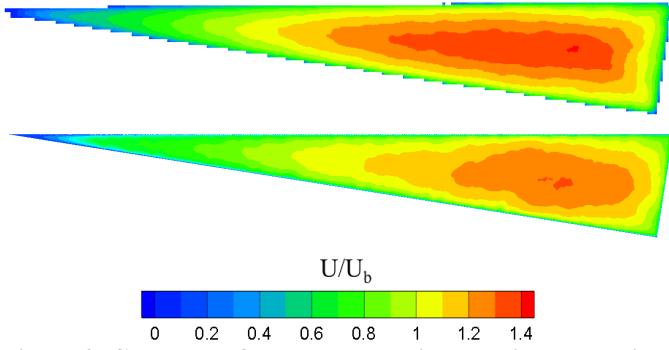
Figure 9. Contours of mean streamwise velocity normalized by bulk velocity. (Top) MRV, (bottom) LES.

The abrupt reduction of the streamwise velocity at the sharp corner is also found in the experimental data of Tung and Irvine [25] for an isosceles triangular channel with an apex angle of 11.5° at Re = 10,600. The ridge where the abrupt velocity change occurs is at $\tau/L = 0.1$ for the current MRV data at Re = 20,000, and at $\tau/L = 0.2$ for the data of [25] at Re = 10,600. The ridge corresponds to the point where turbulence effects diminish, and toward the sharp corner viscous forces dominate as the two walls merge. This was also observed from the data of Daschiel et al. [13], where the ridge occurs at $\tau/L = 0.3$ at Re = 4,500.

Both streamwise velocity profiles steadily increase towards the middle of the channel, but the MRV profile is slightly higher than the LES profile for $0.35 < \tau/L < 0.8$. The profiles follow the pattern observed in the contours of figure 9. The area under the two profiles are similar, which leads to the integrated flow rate (throughout the entire cross section) from MRV closely matching the flow rate from LES, which was specified as a boundary condition.
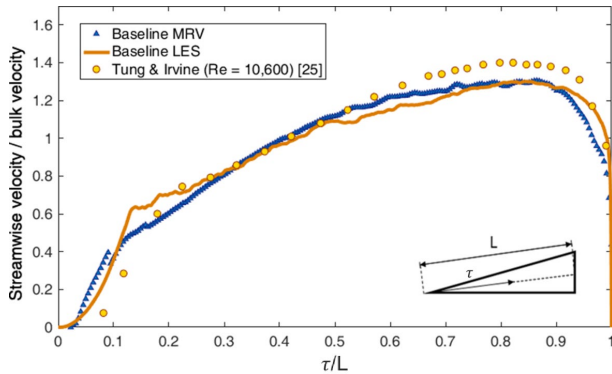

Figure 10. Normalized mean streamwise velocity profile comparison along the centerline of the baseline channel.

Since MRV can only measure mean flow, to further analyze turbulence characteristics in the channel, RMS velocity components from the LES calculations are obtained and shown in figure 11. The RMS velocity components are almost zero from $\tau/L = 0$ to 0.1, meaning that the flow does not fluctuate because it has laminar characteristics. The RMS velocity components are relatively consistent in the middle of the channel for $0.2 < \tau/L <$ 0.8. The transverse components are similar to each other, and gradually increase in this region. Just before the channel wall, for $0.8 < \tau/L < 0.9$, all components are almost equal, which can be considered isotropic turbulence. For $\tau/L > 0.9$, the transverse components slightly increase before rapidly dropping at the wall, while the streamwise component shows a sharp increase up to $U_{RMS}/U_b = 0.18$, before dropping at the wall.

A similar RMS velocity profile is also observed in the DNS data of Daschiel et al. for an isosceles triangular channel with apex angle of 11.5° at Re = 4,500 [13]. The study similarly showed that the turbulent characteristics of the flow disappear when moving towards the corner, resulting in a viscous laminar velocity distribution. Based on these results, we conclude that the narrow apex angle severely limits the flow and dampens the turbulence, which would cause insufficient heat transfer for a sharp turbine blade trailing edge.
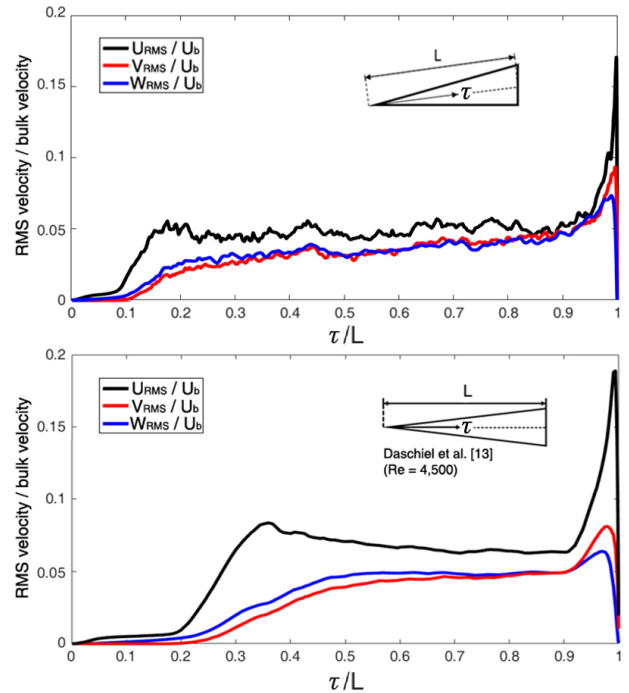

Figure 11. RMS velocity profiles along the centerline of the channel. (Top) current baseline channel at Re = 20,000, (bottom) isosceles triangular channel at Re = 4,500 [13].

Ribbed channel

For the ribbed channel, the mean normalized streamwise velocity is expressed as contours in the cross section, in the same way as the baseline channel (figure 12). The striking difference between the baseline channel is the high velocity near the sharp corner, which is quite a bit higher than the channel center. The fast flow contour in the non-ribbed area is slightly distorted toward the first rib on the bottom, because the flow is sucked into a strong secondary flow locally occurring around the rib. Wakes can also be seen in between the ribs. The two contours are similar, aside from the more prominent inter-rib wake structure for LES. This is likely due to the fact that the spatial resolution

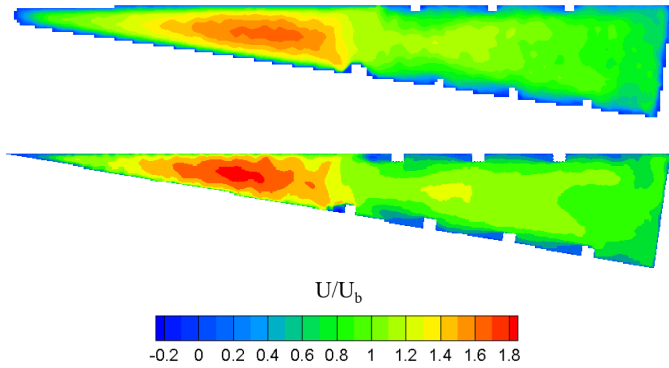is sufficient to resolve the wakes for LES, whereas MRV only has two voxels along the rib height.

Figure 12. Mean streamwise velocity contours for the ribbed channel. (Top) MRV, (bottom) LES.

Figure 13 shows the normalized streamwise velocity at the center line for the ribbed channel with the previous results from the baseline channel. The centerline is defined in the same way as that of the baseline channel. The data trends for MRV and LES are overall fairly similar, with some discrepancies in the high velocity peak region. The normalized flow velocity in the corner at $\tau/L = 0.35$ is higher than that of the center region for the ribbed channel, and also higher than the maximum normalized velocity for the baseline smooth channel. Similar to the baseline channel, there is a sharp decrease in velocity towards the sharp corner. However, the normalized velocity is about 3 times higher than that of the baseline case at the ridge ($\tau/L = 0.1$). Since the flow velocity is much higher in the corner for the ribbed channel, it will correspond to an improvement in heat transfer, compared to the baseline case.
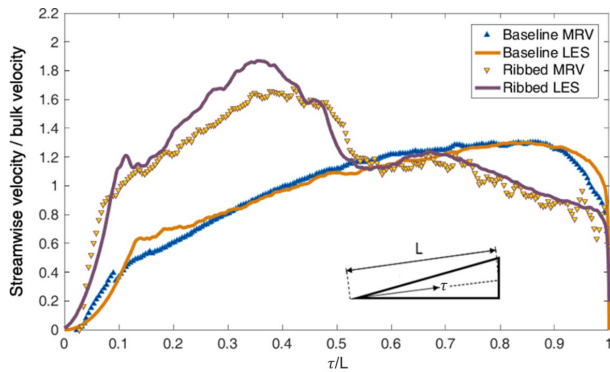

Figure 13. Mean streamwise velocity comparisons between the ribbed channel and baseline channel for MRV and LES.

Figure 14 depicts the normalized RMS velocity profiles from LES. Although notable noises are included due to the short sampling time, about half of the sampling time of the baseline channel case, and geometric complexity of the ribbed channel, the overall profiles adequately reflect the flow behaviors along the centerline. Similar to the baseline channel, the RMS velocity components are trivial at the corner for $\tau/L < 0.1$, and thus the

turbulence remains at a damped state. However, the RMS velocity rapidly increases for $\tau/L > 0.1$ in the apex region. The streamwise component is no longer dominant, and the other two components become similar in magnitude. This is because the ribs have generated a significant amount of three-dimensional turbulence which flows into the corner region, as will be seen from the secondary flow analysis that follows. At $\tau/L = 0.6$, there is a spike in RMS velocity up to almost $0.12U_b$, which is likely due to formation of eddies in the shear layer that forms between the high velocity corner region and low velocity center region.
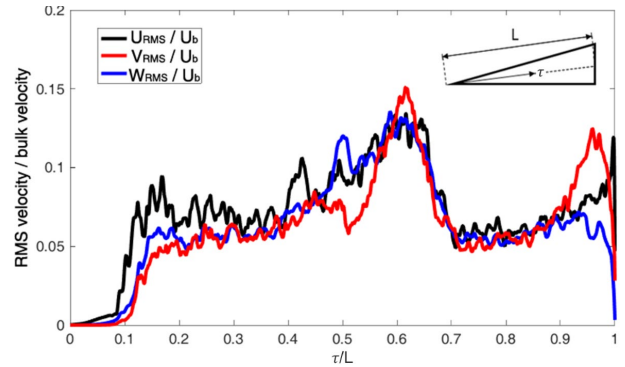

Figure 14. RMS velocity profiles along the centerline of the ribbed channel obtained by LES.

The secondary flow field in the cross section is depicted in figure 15. The contour levels have been chosen to show the normalized velocity in the left to right direction, in order to clearly show the secondary flow structure. The central ribbed area is zoomed in to show how the secondary flow is initiated by the ribs. The secondary flow pattern is similar for the MRV and LES results. As can be seen in figure 15, the secondary flow travels over the ribs in the direction away from the sharp corner, along the bottom and top surfaces. As this flow collides with the right edge, it turns toward the channel center and heads back to the sharp corner. Beyond the ribbed area, in the vicinity of the sharp corner, the secondary flow is reduced and the streamwise velocity becomes the dominant component.
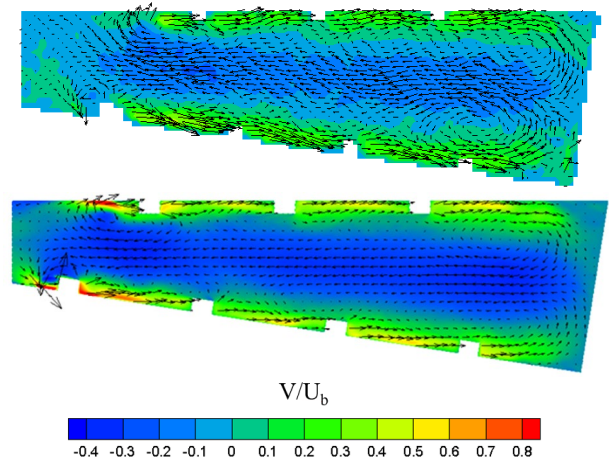

Figure 15. Secondary flow in the cross section. (Top) MRV, (bottom) LES.

To see the effects of the rib on the flow in the streamwise direction, the flow in a plane at a distance 1mm from the ribbed wall of the triangle channel is visualized in figure 16. The mean flow is represented as streamlines. It can be seen that the overall flow pattern is similar between MRV and LES, but there are some slight differences. In the LES results, a separation bubble can clearly be seen behind each rib, emanating from the rib tip near the high-velocity non-ribbed zone. The MRV flow pattern faintly suggests this, but it is not as clear. This is possibly due to the limited capability to detect highly turbulent regions for MRV. The flow between the ribs moves along the rib as a whole, and merges with the streamwise flow toward the far edge of the channel. The flow merging effect seems to be a little more prominent for the LES case.
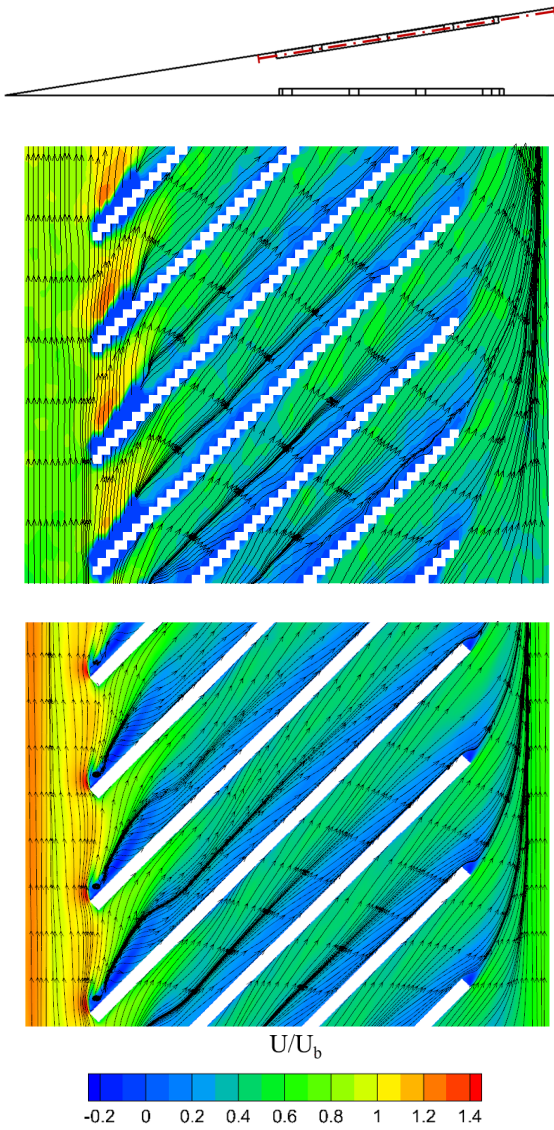
The streamwise flow at the center plane of the ribbed channel is depicted in figure 17. The flow velocity is small toward the sharp corner at the left side of the image, then rapidly increases in the non-ribbed region. In the ribbed region in the right side of the image, there is a sharp drop in flow velocity. Since the secondary flow at the center plane is toward the sharp corner (figure 16), the streamlines veer toward this direction. Results are overall similar for MRV and LES.
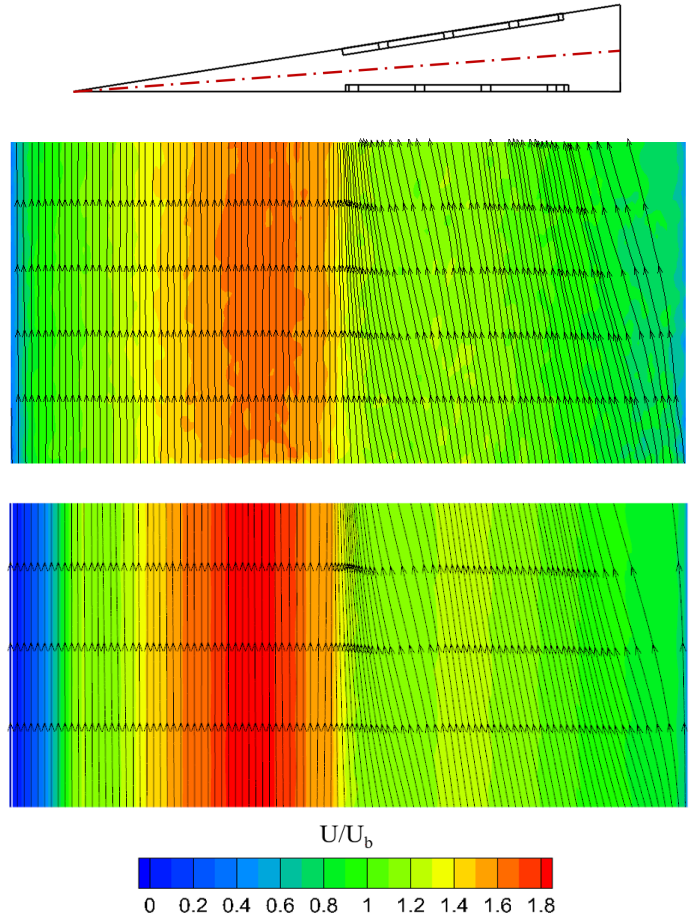

Figure 17. Streamwise velocity contours in the center plane of the ribbed channel. (Top) MRV, (bottom) LES.

Figure 16. Streamwise velocity contours with streamlines on a plane near the ribbed wall. (Top) MRV, (bottom) LES.

CONCLUSION

The flow in a triangular trailing edge internal cooling passage is examined via experimental and numerical methods. A smooth baseline channel and staggered ribbed channel are investigated to evaluate the effect of surface ribs on the overall flow structure inside the triangular channel.

The friction factor was analyzed to ensure the validity of numerical analysis, and to compare how the pressure loss of the ribbed channel increased compared to the baseline channel. The friction factor converges when a fine grid system is adopted, and it agrees fairly well with the Carlson-Irvine correlation for the baseline case. It was also confirmed that the friction factor of the

9

ribbed channel is 13% higher than the baseline channel at the same Reynolds number.

The MRV and LES results indicated an abrupt decrease of flow velocity and turbulence at the sharp corner for the baseline channel, because the effect of the viscous layer becomes prevalent throughout the entire flow region as the pressure and suction side surfaces merge. This would have a detrimental effect on heat transfer at the trailing edge. When ribs are added, the flow velocity near the sharp corner increased substantially, beyond the maximum flow velocity for the baseline channel. The transverse RMS velocities became similar to the streamwise component, as the turbulence is enhanced in all directions due to the ribs. The reason for the increase in velocity near the sharp corner for the ribbed channel is due to secondary flow. Near the wall, the flow is guided by the ribs away from the sharp corner. However, as it meets the far edge, it turns toward the center of the channel and heads into the non-ribbed sharp corner region. As a result of this, the convective heat transfer at the sharp trailing edge corner is expected to be improved when staggered ribs are added to the pressure and suction side internal surfaces. This study also demonstrated that MRV can be used as an experimental tool to validate 3D flow simulations from LES.

ACKNOWLEDGMENTS

REFERENCES

[1] Saxer-Felici, H., Naik, S., Gritsch, M., 2013, "Heat transfer characteristics of a blade trailing edge with pressure side bleed extraction", Proc. of ASME Turbo Expo 2013, San Antonio, Texas, USA, GT2013-95003

[2] Benson, M. J., Elkins, C. J., Yapa, S. D., Ling, J. B., Eaton, J. K., 2012, "Effects of varying Reynolds number, blowing ratio, and internal geometry on trailing edge cutback film cooling", Experiments in Fluids, 52(6), pp. 1415-1430.

[3] Benson, M. J., Elkins, C. J., Eaton, J. K., 2011, "Measurements of 3D velocity and scalar field for a film-cooled airfoil trailing edge", Experiments in Fluids, 51(2), pp. 443-455.

[4] Chen, Y., Matalanis, C. G., Eaton, J. K., 2008, "High resolution with various internal cooling designs", Journal of Turbomachinery, 128(1), pp. 196-205.

[6] Martini, P., Schulz, A., Bauer, H. J., Whitney, C. F., 2006, "Detached eddy simulation of film cooling performance on the trailing edge cutback PIV measurements around a model turbine blade trailing edge film-cooling breakout", Experiments in Fluids, 44(2), pp. 199-209.

[5] Martini, P., Schulz, A., Bauer, H. J., 2006, "Film cooling effectiveness and heat transfer on the trailing edge cutback of gas turbine airfoils of gas turbine airfoils", Journal of Turbomachinery, 128(2), pp. 292-299.

[7] Mucignat, C., Armellini, A., Casarsa, L., 2013, "Flow field analysis inside a gas turbine trailing edge cooling channel under static and rotating conditions: Effect of ribs", International Journal of Heat and Fluid Flow, 42, pp. 236-250.

[8] Armellini, A., Coletti, F., Arts, T., Scholtes, C., 2010, "Aerothermal investigation of a rib-roughened trailing edge channel with crossing-jets—part I: flow field analysis", Journal of Turbomachinery, 132(1), pp. 011009-011009-9.

[9] Coletti, F., Armellini, A., Arts, T., Scholtes, C., 2011, "Aerothermal investigation of a rib-roughened trailing edge channel with crossing jets—part II: heat transfer analysis", Journal of Turbomachinery, 133(3), pp. 024-031.

[10] Schneider, H., Von Terzi, D. A., Bauer, H. J., Rodi, W., 2015, "Coherent structures in trailing-edge cooling and the challenge for turbulent heat transfer modelling", International Journal of Heat and Fluid Flow, 51, pp. 110-119.

[11] Eckert, E. R. G., Irvine, T. F., 1960, "Pressure drop and heat transfer in a duct with triangular cross section", Journal of Heat Transfer, 82(2), pp. 125-136.

[12] Hiromoto, U., Yuji, S., Hiromichi, F., 1982, "Turbulence measurements and mass transfer in fully developed flow in a triangular duct with a narrow apex angle", International Journal of Heat and Mass Transfer, 25(5), pp. 615-624.

[13] Daschiel, G., Frohnapfel, B., Jovanović, J., 2013, "Numerical investigation of flow through a triangular duct: The coexistence of laminar and turbulent flow", International Journal of Heat and Fluid Flow, 41, pp. 27-33.

[14] White, F. M., 2016, Fluid mechanics (8th ed. in SI Units), New York: McGraw-Hill, p. 325.

[15] Lee, J., Ko, S., Cho, J. H., Song, S., 2017, "Validation of magnetic resonance velocimetry for mean velocity measurements of turbulent flows in a circular pipe", Journal of Mechanical Science and Technology, 31(3), pp. 1275-1282.

[16] Elkins, C. J., Markl, M., Pelc, N., Eaton, J. K., 2003, "4D Magnetic resonance velocimetry for mean velocity measurements in complex turbulent flows", Experiments in Fluids, 34(4), pp. 494-503.

[17] Pelc, N. J., Sommer, F. G., Li, K. C., Brosnan, T. J., Herfkens, R. J., Enzmann, D. R., 1994, "Quantitative magnetic resonance flow imaging", Magnetic Resonance Quarterly, 10(3), pp. 125-147.

[18] Siekman, M., Helmer, D., Hwang, W., Laskowski, G., Tan, E. T., Natsui, G., 2014, "A Combined CFD/MRV Study of Flow Through a Pin Bank", Proc. of ASME Turbo Expo 2014, Dusseldorf, Germany, GT2014-25350.

[19] Bruschewski, M., Freudenhammer, D., Buchenberg, W. B., Schiffer, H. P., Grundmann, S., 2016, "Estimation of the measurement uncertainty in magnetic resonance

velocimetry based on statistical models", Experiments in Fluids, 57(5), pp 83.

[20] Kim, J., Kim, D., Choi, H., 2001, "An immersed-boundary finite-volume method for simulations of flow in complex geometries", Journal of Computational Physics, 171(1), pp. 132-150.

[21] Park, N., Lee, S., Lee, J., Choi, H., 2006, "A dynamic subgrid-scale eddy viscosity model with a global model coefficient", Physics of Fluids, 18(12), pp. 109-125.

[22] Ahn, J., Choi, H., Lee, J. S., 2004, "Large eddy simulation of flow and heat transfer in a channel roughened by square or semicircle ribs", Proc. of ASME Turbo Expo 2004: Power for Land, Sea, and Air, Vienna, Austria, pp. 411-418

[23] Davidson, L., 2009, "Large eddy simulations: how to evaluate resolution", International Journal of Heat and Fluid Flow, 30(5), pp. 1016-1025.

[24] Carlson, L. W., Irvine, T. F., 1961, "Fully developed pressure drop in triangular shaped ducts", Journal of Heat Transfer, 83(4), pp. 441-444.

[25] Tung, S. S., Irvine, T. F., 1979, Studies in Heat Transfer, New York: McGraw-Hill, p. 309.